The Astrophysical Journal, 631:399–410, 2005 September 20

AN INFALLING TORUS OF MOLECULAR GAS AROUND THE ULTRACOMPACT H II REGION G28.20−0.05

Peter K. Sollins, Qizhou Zhang, Eric Keto, and Paul T. P Ho
Harvard-Smithsonian Center for Astrophysics, 60 Garden Street, Cambridge, MA 02138; psollins@cfa.harvard.edu
Received 2005 April 22; accepted 2005 June 2

ABSTRACT

We present new observations of the ultracompact H II region G28.20−0.05 in the 23 GHz continuum and the $NH_3(1, 1)$, $NH_3(2, 2)$, and $NH_3(3, 3)$ lines. To explain the complicated kinematics of the molecular gas, we propose a model consisting of two components. One component is an infalling, equatorial torus of molecular gas, whose dense central region has been ionized to form the ultracompact H II region. The second component is a larger expanding molecular shell driven by some type of wide-angle outflow or wind. We estimate that the infall component includes more than 18 $M_\odot$ of molecular gas. We calculate the central mass to be 79 $M_\odot$, probably comprising more than one star. The arrangement of the molecular material suggests a connection to the other disklike structures seen around massive young stars. The central star in this case is more massive, and the whole region may be more evolved than other similar objects such as IRAS 20126+4104, IRAS 18089−1732, G192.16−3.84, and AFGL 5142.

Subject headings: accretion, accretion disks — H II regions — ISM: individual (G28.20−0.05) — ISM: molecules — stars: formation

1. INTRODUCTION

Much research has been done attempting to extend the now well-defined process of low-mass star formation to intermediate- and high-mass star formation. The accepted standard model for low-mass star formation, as described in Shu et al. (1987), involves a molecular cloud core that collapses to form a protostar with an accretion disk. A bipolar outflow forms, and accretion through the disk slows. Eventually, the cloud is dispersed and the protostar quasi-statically contracts onto the main sequence, radiating away its gravitational energy. Kahn (1974), however, pointed out that, because of their enormous luminosity, the Kelvin-Helmholtz timescale for contraction of a massive star is much shorter than for low-mass stars. Massive stars may radiate away their gravitational energy so quickly that they approach the main sequence and become very luminous before the surrounding protostellar envelope has finished collapsing (Garay & Lizano 1999). Kahn (1974) and Wolfire & Cassinelli (1987) calculated that in this case the pressure of the stellar radiation may be adequate to stop accretion under certain circumstances. Observationally, however, several examples are now known of stars or protostars with masses of order 10 $M_\odot$ or less, i.e., early B-type stars, which appear to be undergoing accretion through a disk (Zhang et al. 1998b, 2002; Shepherd & Kurtz 1999; Chini et al. 2004; Beuther et al. 2004). Most of these sources are known to also include an outflow. Thus, some aspects of the highly successful standard model of low-mass star formation have been observed in stars up to stellar masses of 10 $M_\odot$, despite the potential radiation pressure problem.

At the high end of the mass scale, a very different type of accretion scenario has been proposed to explain observations of the ultracompact (UC) H II region G10.6−0.4. The ionized gas in G10.6 has a radius of about 6000 AU (0.03 pc) and contains a grouping of massive young stars with a luminosity of 9.2×10^5 $L_\odot$, with a mass of 150 $M_\odot$, and emitting 2.2×10^{50} Lyman continuum photons per second, including at least one early O-type star (Sollins et al. 2005). Outside the UC H II region, molecular gas can be seen to be infalling and rotating in absorption in the $NH_3(3, 3)$ line (Ho & Haschick 1986; Keto et al. 1987, 1988). This molecular accretion flow proceeds all the way up to the ionization front (Sollins et al. 2005). In the ionized gas, H66α observations show that the ionized gas is also moving inward and settling into an ionized disk in the center of the UC H II region (E. Keto 2005, in preparation). Keto (2002b) proposed a model in which the ionized gas is gravitationally trapped by the mass of the central stars, allowing the molecular accretion flow to pass through a stalled ionization front and continue as an ionized accretion flow. The particular combination of mass and luminosity of the stellar cluster, and angular momentum in the molecular gas puts G10.6 in a regime in which the thermal pressure of the ionized gas is confined by the gravitational force of the central stars, and the molecular gas does not settle into a disk, but rather a rotating, somewhat flattened, quasi-spherical accretion flow. This is a very different scenario from the low-mass standard model in which molecular gas accretes quasi-statically through a rotationally supported accretion disk.

In order to investigate a regime of massive star formation in between the grouping of O stars in G10.6 and the individual early B-type stars seen to have disks and outflows, we have observed G28.20−0.05. G28 is an UC H II region at a distance of $5.7^{+0.5}_{-0.8}$ kpc (Fish et al. 2003), with a radius of about 3400 AU (0.017 pc). Using the formula of Casoli et al. (1986), the far-infrared luminosity based on *IRAS* fluxes is 1.6×10^5 $L_\odot$, corresponding to one O8 V star, which would have a mass of 31 $M_\odot$ and an ionizing flux of 7.4×10^{48} Lyman continuum photons per second (Vacca et al. 1996). Of course, if more than one star is present, the luminosity does not uniquely determine the mass or flux of ionizing photons. Using a broader range of infrared measurements, Walsh et al. (2003) get 1.8×10^5 $L_\odot$, consistent with the Casoli et al. (1986) value when scaled to our assumed distance. When compared to G10.6, G28 has a lower luminosity, smaller radius, and presumably different central mass. These factors should put G28 into a different accretion regime than the previous work described above.

2. OBSERVATIONS

We observed the UC H II region G28.20−0.05 with the NRAO Very Large Array (VLA)[1] on four occasions in 2003, with

[1] The National Radio Astronomy Observatory is a facility of the National Science Foundation operated under cooperative agreement by Associated Universities, Inc.

TABLE 1
THE DATA

Date	Line	Energy[a] (K)	Array	Beam (arcsec)	Δv (km s^{-1})	rms (mJy beam^{-1})
2003 Feb 14.....	(1, 1)	23.4	D	4.0 × 2.6	0.6	5.2
2003 Feb 14.....	(2, 2)	64.9	D	4.0 × 2.6	0.6	5.2
2003 May 27.....	(3, 3)	125	D	3.1 × 2.4	0.3	3.4
2003 Oct 9.....	(2, 2)	64.9	BnA	0.34 × 0.23	0.6	4.1
2003 Oct 10.....	(3, 3)	125	BnA	0.39 × 0.30	0.6	3.9

[a] Ho & Townes (1983).

the phase center at $\alpha(\mathrm{J2000.0}) = 18^{\mathrm{h}}42^{\mathrm{m}}58\overset{\mathrm{s}}{.}10$, $\delta(\mathrm{J2000.0}) = -4^{\circ}13'57\overset{''}{.}87$. We observed the (1, 1), (2, 2), and (3, 3) inversion lines of NH_3 in the D configuration, yielding a resolution of about 3″ in natural-weighted maps. We also observed the (2, 2) and (3, 3) lines in the hybrid BnA configuration yielding a resolution of about 0.″3 in uniform-weighted maps.

We observed 3C 286 to set the absolute flux scale, and 1849+005 to calibrate the phases. The passband response was calibrated using 3C 273 for the (1, 1) and (2, 2) D-array data, and 3C 454.3 for the rest of the data. After initial flux and phase calibration, all visibilities were also self-calibrated for phase and amplitude, using as the model a map made from the velocity-integrated visibilities. The resolutions and noise levels, as well as some physical parameters of the lines observed, in each of the maps are listed in Table 1.

As in earlier work on the inversion lines of NH_3 as seen around UC H II regions (Keto et al. 1988; Sollins et al. 2005), we make this point regarding spatial resolution and the detectability of the line in either emission or absorption. We achieve a typical sensitivity in a single channel of the line data of 4 mJy beam^{-1}. At a resolution of 3″, this flux sensitivity means that the 3 σ detection limit in terms of temperature is about 4 K. So thermal emission of any appreciable optical depth from a hot molecular core whose actual temperature is around 100 K should be easily detectable. For the higher resolution data, the flux sensitivity is similar, but the synthesized beam is a factor of 10 smaller, resulting in a factor of 100 worse temperature sensitivity. No thermal emission, at any optical depth, will be detectable from a 100 K hot molecular core when the 3 σ detection limit is 400 K, as in the 0.″3 resolution data. The sensitivity to absorption, however, is quite high in the high-resolution maps. Our continuum map, based on the BnA-array (2, 2) data, has a peak brightness temperature of 7500 K. The 1 σ noise level in the line channel maps is 130 K, so very optically thick absorption could be detected at signal-to-noise ratios exceeding 50. We thus expect to detect both line absorption and emission in the D-array data, but only absorption in the BnA-array data.

3. RESULTS

3.1. *The High-Resolution Data*

The continuum map derived from the BnA-array $NH_3(2, 2)$ observations is shown in Figure 1. The source is resolved and there are two peaks separated by 0.″4, just over one synthesized beam. At the 50% contour, the continuum emission is 0.″6 × 0.″8. The total flux in the central continuum source is 0.98 Jy. The peak is 181 mJy beam^{-1}, corresponding to a brightness temperature of 5700 K. Assuming the electron temperature is 10,000 K, the peak optical depth is $\tau_\nu = 0.84$, and the peak emission measure is 2.0×10^9 pc cm^{-6}. Assuming uniform density and a recombination coefficient of 3×10^{-13} cm^3 s^{-1} (Keto 2003), the electron density is 2.1×10^6 cm^{-3}, the mass of ionized gas is 0.54 $M_\odot$, and the flux of ionizing photons necessary to balance recombinations in the UC H II region is 1.6×10^{49} s^{-1}. If from a single star, this ionizing flux would correspond to a O6.5 V star of mass 41 $M_\odot$ and luminosity 3.1×10^5 $L_\odot$. Since this does not match the known luminosity, we suspect that the central object is a multiple star system, with no stellar member as early as O6.5. It should also be noted that there are several assumptions in this calculation (temperature of the ionized gas, path length associated with the observed continuum flux, and uniform density structure) that could change the resulting spectral type.

The key feature of our BnA-array line data is that it divides neatly into two distinct components, one centered at 90 km s^{-1}, which we associate with an outflow or expansion, and one centered at 97 km s^{-1}, which we associate with infall. The two components are clearly separated in the $NH_3(2, 2)$ position-velocity diagrams in Figures 2–4. The lower resolution data fix the ambient velocity of the cloud at 95.5 km s^{-1}, so one component is blueshifted, while the other is redshifted, hence the infall and outflow interpretation. Figures 5 and 6 also help to distinguish the two components and are discussed in detail below.

3.1.1. *The* 90 km s^{-1} *Outflow Component*

The outflow component is cool and optically thin. It is detected over the entire face of the continuum source, and its mean velocity varies little as a function of position. The first and second moments of the 90 km s^{-1} component can be seen in the first two panels in Figure 5. The moments of the 90 km s^{-1} component are integrated from 84 to 92 km s^{-1}. Compared to the 97 km s^{-1} component, both moments of the 90 km s^{-1} component vary little with position. But as seen in Figure 6, the first moment of the 90 km s^{-1} component does have a clear pattern. The velocity pattern shows parallel stripes monotonically increasing from 89.7 km s^{-1} on one side to 91.4 km s^{-1} on the other side. The optical depth of the line in the 90 km s^{-1} component is relatively low. There is no detectable absorption in the first satellite hyperfine line corresponding to the 90 km s^{-1} component, meaning that the optical depth in the main line is everywhere less than 2.7. Because the 90 km s^{-1} component is detected in (2, 2) but not (3, 3), we can put an upper limit on its temperature of 30 K. It is important to note that the 90 km s^{-1} component extends over the entire face of the UC H II region.

3.1.2. *The* 97 km s^{-1} *Infall Component*

The rest of the panels in Figure 5 show the kinematics of the 97 km s^{-1} component. The most prominent feature in Figure 5 is the sharp northwest-southeast line in the BnA-array maps of the first and second moments. This is the edge of the 97 km s^{-1} component. Because the 90 km s^{-1} component extends over the

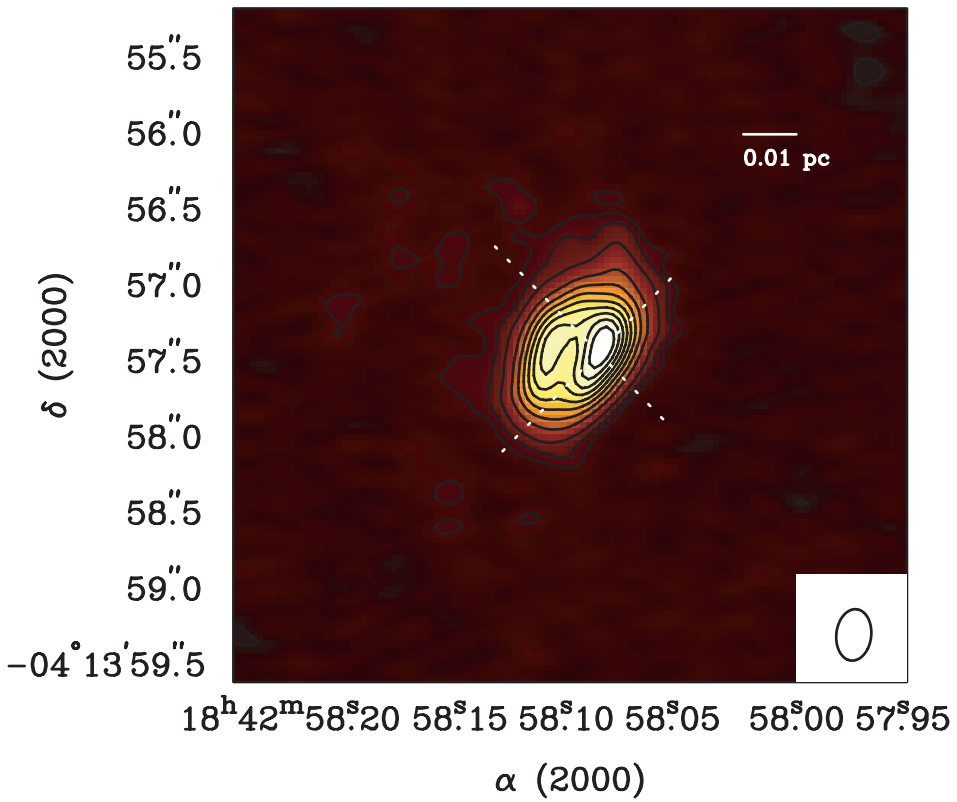

FIG. 1.—Plot of the 23 GHz continuum image of G28.20−0.05. The contours are at 2.5%, 5%, 10%, 20%, 30%, 40%, 50%, 60%, 70%, 80%, and 90% of the peak, 181 mJy beam^{-1}. The color scale is linear from −10 to 181 mJy beam^{-1}. The dotted white lines indicate the position-velocity cuts shown in Figs. 2–4. The synthesized beam is shown in the lower right.

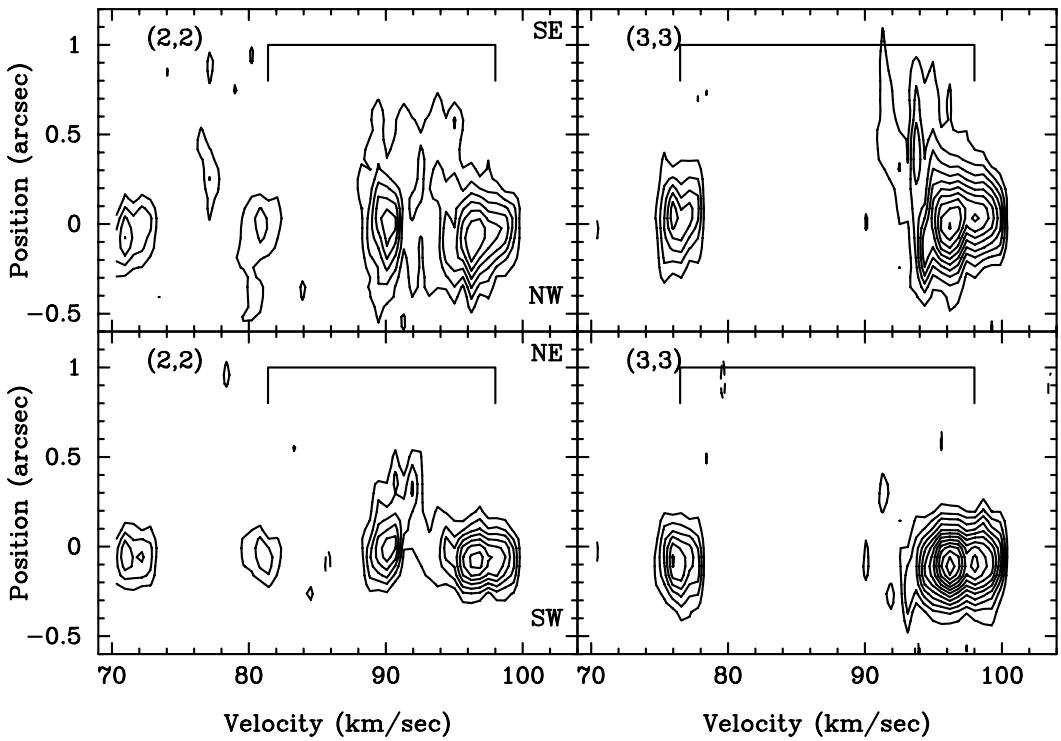

FIG. 2.—Position-velocity diagrams in the $NH_3(2, 2)$ and $NH_3(3, 3)$ absorption lines. The cuts are northwest-southeast (NW-SE) in the top row and northeast-southwest (NE-SW) in the bottom row. The position origin is at the continuum peak. The contours are multiples of 10 mJy beam^{-1}. Higher contours indicate deeper absorption, with solid contours used instead of dashed lines for clarity. The (2, 2) line clearly shows the two different components, while the (3, 3) line does not show the 90 km s^{-1} component. The separations of the main hyperfine component and the inner satellite component are shown for both lines.

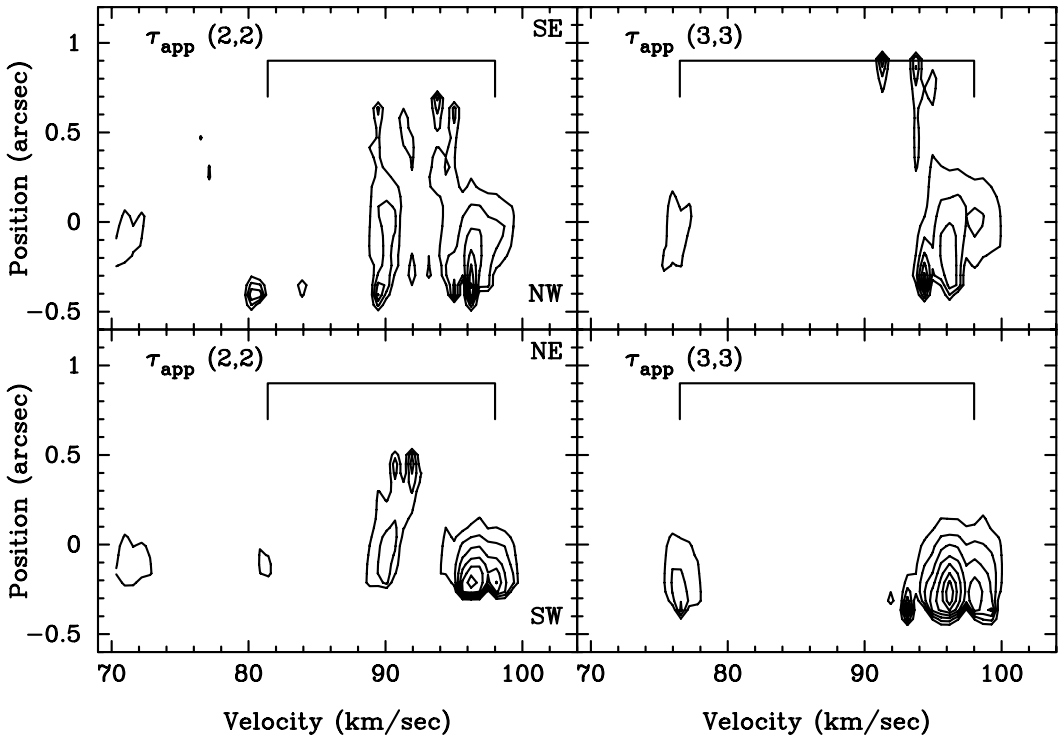

FIG. 3.—Position-velocity diagrams in the apparent optical depth of the $NH_3(2, 2)$ and $NH_3(3, 3)$ lines. The cuts are northwest-southeast (NW-SE) in the top row and northeast-southwest (NE-SW) in the bottom row. The position origin is at the continuum peak. The optical depth contours are multiples of 0.1. The (2, 2) line clearly shows the two different components, while the (3, 3) line does not show the 90 km s^{-1} component. The separations of the main hyperfine component and the inner satellite component are shown for both lines.

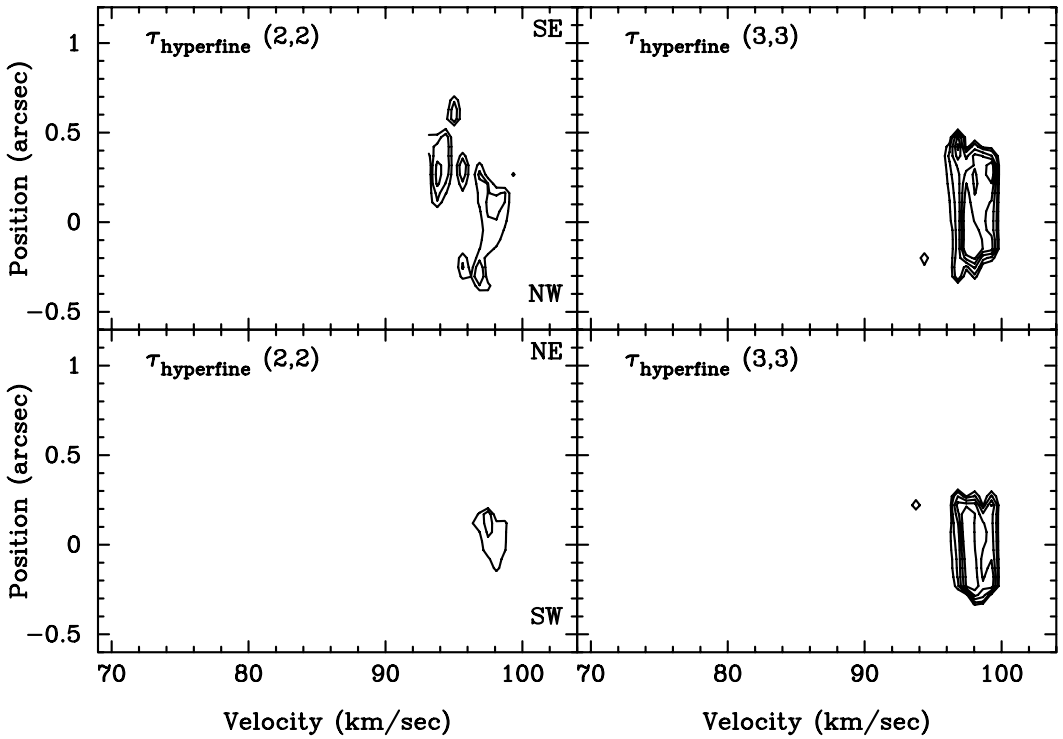

FIG. 4.—Position-velocity diagrams in the hyperfine optical depth of the $NH_3(2, 2)$ and $NH_3(3, 3)$ lines. The cuts are northwest-southeast (NW-SE) in the top row and northeast-southwest (NE-SW) in the bottom row. The position origin is at the continuum peak. The optical depth contours are multiples of 4. The measurement of hyperfine optical depth requires the detection of the satellite hyperfine component. Hence lower optical depth material, detectable in apparent optical depth or in the raw absorption line, is suppressed here.

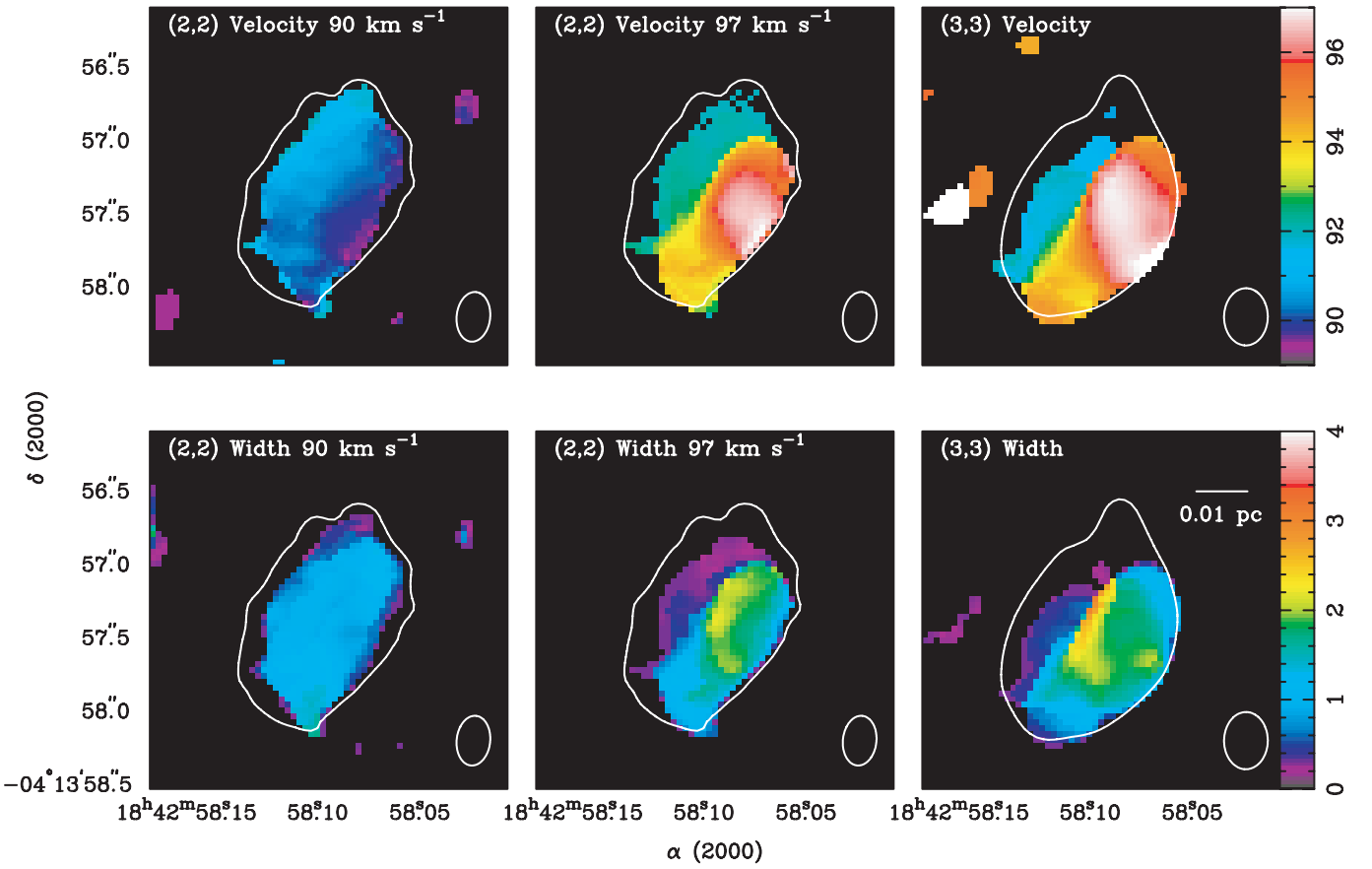

FIG. 5.—First and second moments of the NH_3 (2, 2) and (3, 3) lines in color and the continuum maps in contours. The contour is 5% times the continuum peaks, 188 mJy beam^{-1} in the (2, 2) continuum image and 305 mJy beam^{-1} in the (3, 3) continuum image, which has a larger beam. The velocities are indicated by the color bars in km s^{-1}. The first moment is the flux-weighted mean velocity of the line, labeled "velocity," and the second moment is the flux-weighted dispersion, σ, or 0.425 times the FWHM for a Gaussian. For the (2, 2) line, moments are first calculated over the range 84–92 km s^{-1}. These moment maps are labeled 90 km s^{-1} and correspond to the 90 km s^{-1} outflow component. The moments are then calculated for the (2, 2) line over the velocity range 92–103 km s^{-1}. These maps are labeled 97 km s^{-1} and correspond to the infall component near 97 km s^{-1}. The moments of the (3, 3) line are calculated over the entire range, since the 90 km s^{-1} component is nearly invisible in (3, 3), and only the infall component is detected. The most striking feature of the data is the sharp line apparent in the moment maps of the infall component. At positions in the northeast of the moment maps of the infall component, we see some leakage of the outflow component into the velocity window used for the infall component. The synthesized beam is shown in the lower right of each panel.

entire face of the continuum emission, we know the sharp line must be due to a cut off in the absorption from the 97 km s^{-1} component. In the direction perpendicular to the edge, the beam is >0.″2, so the sharpness of the edge is striking. This edge suggests the presence of a disklike structure, perhaps a toroid, surrounding the UC H II region. If the toroid were inclined, it would naturally produce absorption over only half of the face of the UC H II region.

The spatial pattern of the mean velocity of the 97 km s^{-1} component shows infall and possibly weak rotation. The pattern, from northwest to southeast, goes from 95 to 97 km s^{-1} and back down to 94 km s^{-1}. This is reminiscent of the "off-center bull's-eye" characteristic of combined infall and rotation discussed in Keto et al. (1988) and observed in G10.6−0.4 (Keto et al. 1987; Keto 2002a; Sollins et al. 2005). If rotation is responsible for the offset of the position of fastest infall, then the axis of rotation must be northeast-southwest, with the projection into the plane of the sky of the angular momentum vector pointing northeast. Position-velocity cuts in both the direction of the axis of rotation (northeast-southwest) and perpendicular to the axis of rotation (northwest-southeast) are shown in Figure 2. The most redshifted infalling gas can be seen at 100 km s^{-1}. While the offset of the position of fastest infall in the first-moment map is conspicuous, it is difficult to see any additional evidence of rotation in the position-velocity diagram.

The infalling gas is warm and very optically thick. Figures 3 and 4 show the same position-velocity cuts as Figure 2, but in the apparent optical depths, and the hyperfine optical depths instead of in the actual line absorption. (For an explanation of apparent and hyperfine optical depths, see the Appendix.) The separations between the main hyperfine component and first satellite hyperfine component are 16.6 and 21.5 km s^{-1} for the (2, 2) and (3, 3) lines, respectively, and in the (2, 2) line the outer satellite line is at a separation of 25.8 km s^{-1}. Only the most optically thick gas could ever be detected in the much weaker satellite lines. It is the redshifted, infalling gas that is detectable in the satellite lines and is the most optically thick. Since infall models generally predict strong central condensation (Shu 1977; Terebey et al. 1984), we expect the most redshifted infalling gas to be the densest, and most optically thick, and it is, with peak hyperfine optical depths of 16 in the (2, 2) line and 47 in the (3, 3) line. The (2, 2) and (3, 3) peak optical depths correspond to a rotational temperature of 280 K, much warmer than the 30 K upper limit for the outflow component, which is detected only in (2, 2). Using the 280 K temperature and an abundance of NH_3 relative to H_2 of 10^{-7}, we calculate the mass of the

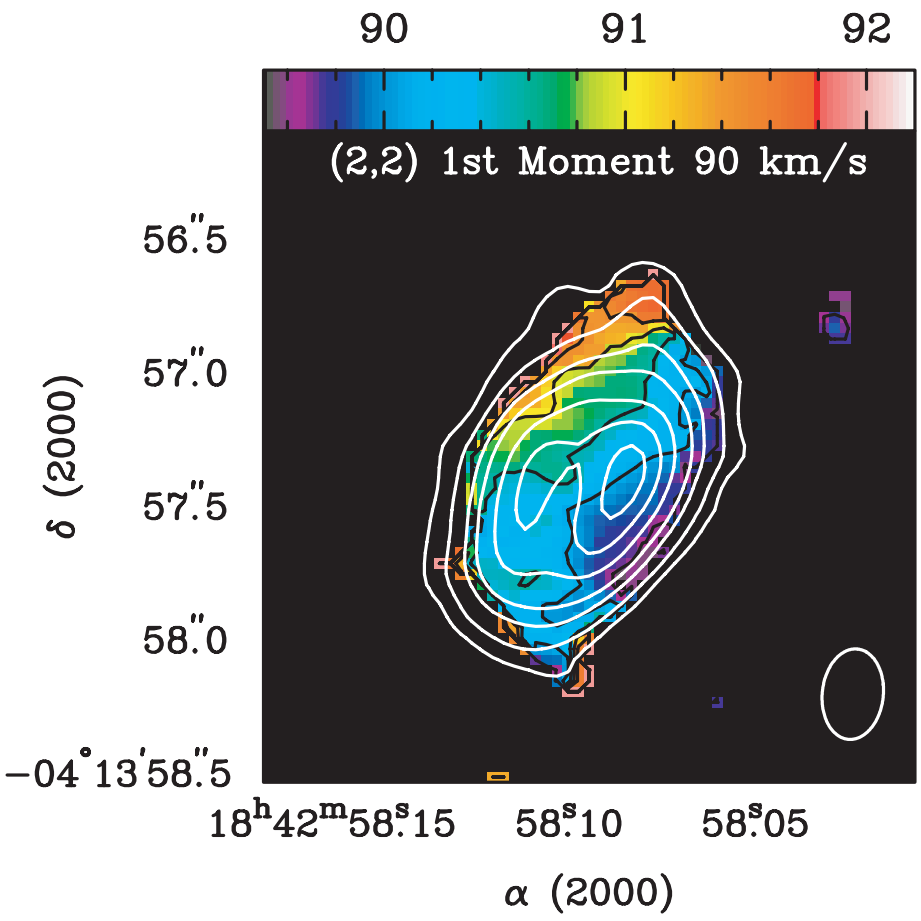

FIG. 6.—First moment of the 90 km s^{-1} component of the $NH_3(2, 2)$ line over the velocity range $v_{lsr} = 84-92$ km s^{-1}. The colors represent the mean velocity of the line and run from 89.4 to 91.8. The black contours also show the velocity field. The white contours are the continuum map based on the (2, 2) observations with contours at 10%, 20%, 30%, 50%, 70%, and 90% times 188 mJy beam^{-1}. The synthesized beam is shown at the lower right.

gas detected in the infall component to be 9 $M_\odot$, using either the (3, 3) or the (2, 2) optical depth, i.e., the two lines are consistent. Note that this is only a fraction of the mass of the entire infall component, since only that part of the infall component that lies in front of the continuum source can be observed. Thus, mass of the infall component should be at least 18 $M_\odot$, or perhaps more. The largest source of uncertainty here is the abundance, which may be uncertain by as much as an order of magnitude.

3.2. *The Low-Resolution Data*

The molecular core surrounding the UC H II is detected in all three lines we observed in the low angular resolution mode and shows typical evidence of internal heating. Figure 7 shows 3″ resolution, velocity-integrated maps in all three lines. The (1, 1) map includes the most extended emission, while the (3, 3) emission is the most compact. This is consistent with central heating of the molecular core from the UC H II region, similar to the molecular gas in the regions surrounding massive protostars, such as AFGL 5142 (Zhang et al. 2002). All three line maps show two peaks immediately next to the UC H II region, the brighter to the northeast, the fainter to the southwest. We use these peaks to define an axis for a position-velocity cut running from 30° west of south to 30 east of north. The more extended emission runs northwest to southeast, so we use that to define another position-velocity cut. Both cuts are indicated in Figure 7. The absorption toward the UC H II region can be seen in (2, 2) and (3, 3) as negative contours at the center of the zeroth-moment maps.

The position-velocity cut in the (1, 1) data establishes the velocity of the ambient cloud. Figure 8 shows the position-velocity cuts indicated in Figure 7. The first satellite hyperfine components of the $NH_3(1, 1)$ line are separated from the main line by ±7.8 km s^{-1}, and the main line has an intrinsic line strength only 3.6 times that of the inner satellites. Since the kinematics in this object involve relative velocities greater than 8 km s^{-1}, and since the satellite lines can be seen strongly in emission, the position-velocity diagrams for the (1, 1) line are confusing, with strong blending of the main line and the inner satellites. Near the UC H II region, it is impossible to tell where emission and absorption from the different hyperfine components are blending. However, even in the (1, 1) position-velocity diagrams, away from the UC H II region, one can see the gas returning to its ambient velocity, around 95.5 km s^{-1}, shifting to about 97 km s^{-1} in the far southeast of the cloud.

In the (2, 2) and (3, 3) position-velocity diagrams, the kinematics are less confused, showing the same outflow component detected at high angular resolution. Off the UC H II region, most of the emission is near the ambient velocity, 95.5 km s^{-1}. At the position of the UC H II region we see several components in the main line, separated in velocity. There is blueshifted absorption in both (2, 2) and (3, 3) detectable from 88 to 93 km s^{-1}. There is also high-velocity redshifted emission out to 105 km s^{-1}. The absorption is the same outflow component detected in the high-resolution data, and the emission is the back side of the outflow, which could not be detected at high resolution. At the position of the UC H II region, the apparent optical depths at 90 km s^{-1} in

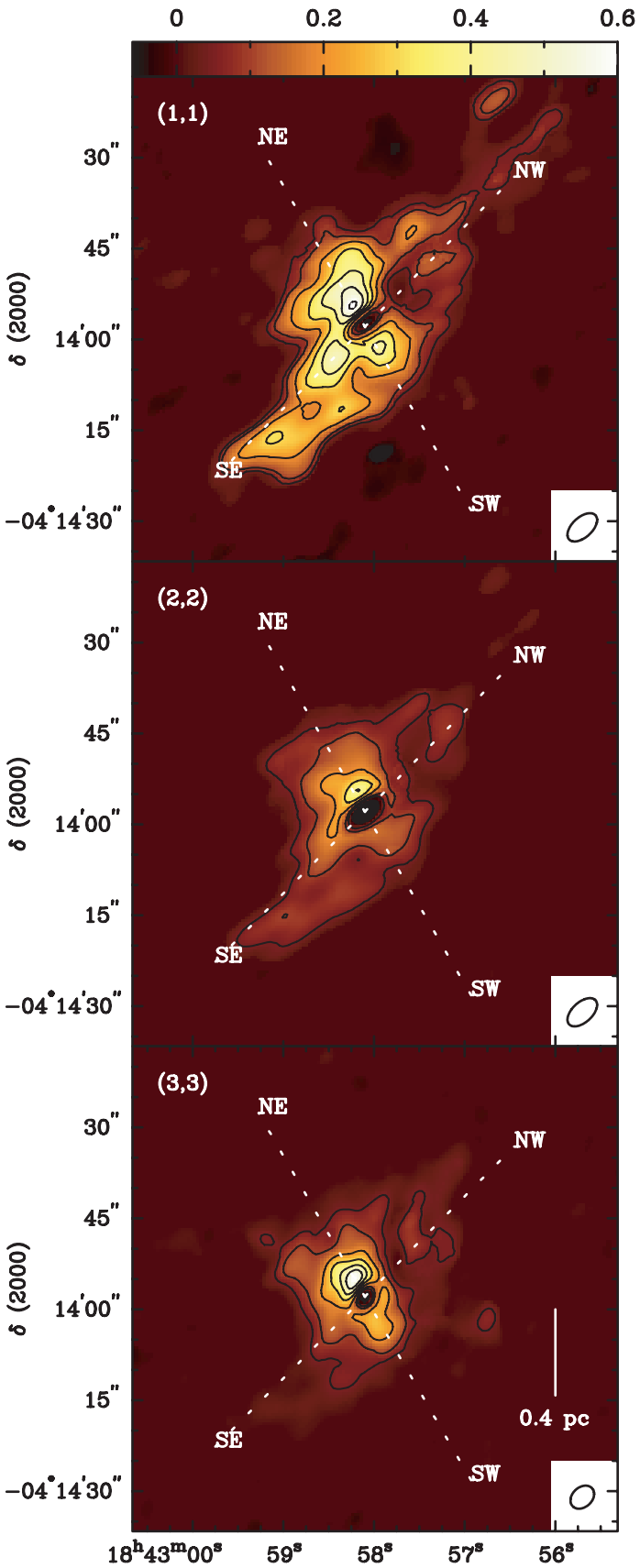

FIG. 7.—Maps of the velocity-integrated line strength in the (1, 1), (2, 2), and (3, 3) lines of NH_3 at 3″ resolution. The color scale runs from −0.06 to 0.6 Jy beam^{-1} km s^{-1}, and the contours are at 0.05, 0.1, 0.2, 0.3, 0.4, 0.5, and 0.6 Jy beam^{-1} km s^{-1}. The (1, 1), (2, 2) and (3, 3) states are 23, 65, and 125 K above ground, respectively. The coldest gas is seen in NH_3(1, 1) and is the most extended. The warmest gas is closer to the UC H II region. Because three of the hyperfine components of the (1, 1) line are confused, the line is shown integrated over all three lines, from 80 to 100 km s^{-1}. The (2, 2) and (3, 3) lines are integrated from 85 to 106 km s^{-1} so as to include only the main line. The synthesized beam is indicated in the lower right of each panel. The dotted white lines indicate the positions of the position-velocity cuts shown in Fig. 8. One cut goes through the more extended gas, directly northwest to southeast. The other cut goes through the two emission peaks, 30° west of south to 30° east of north.

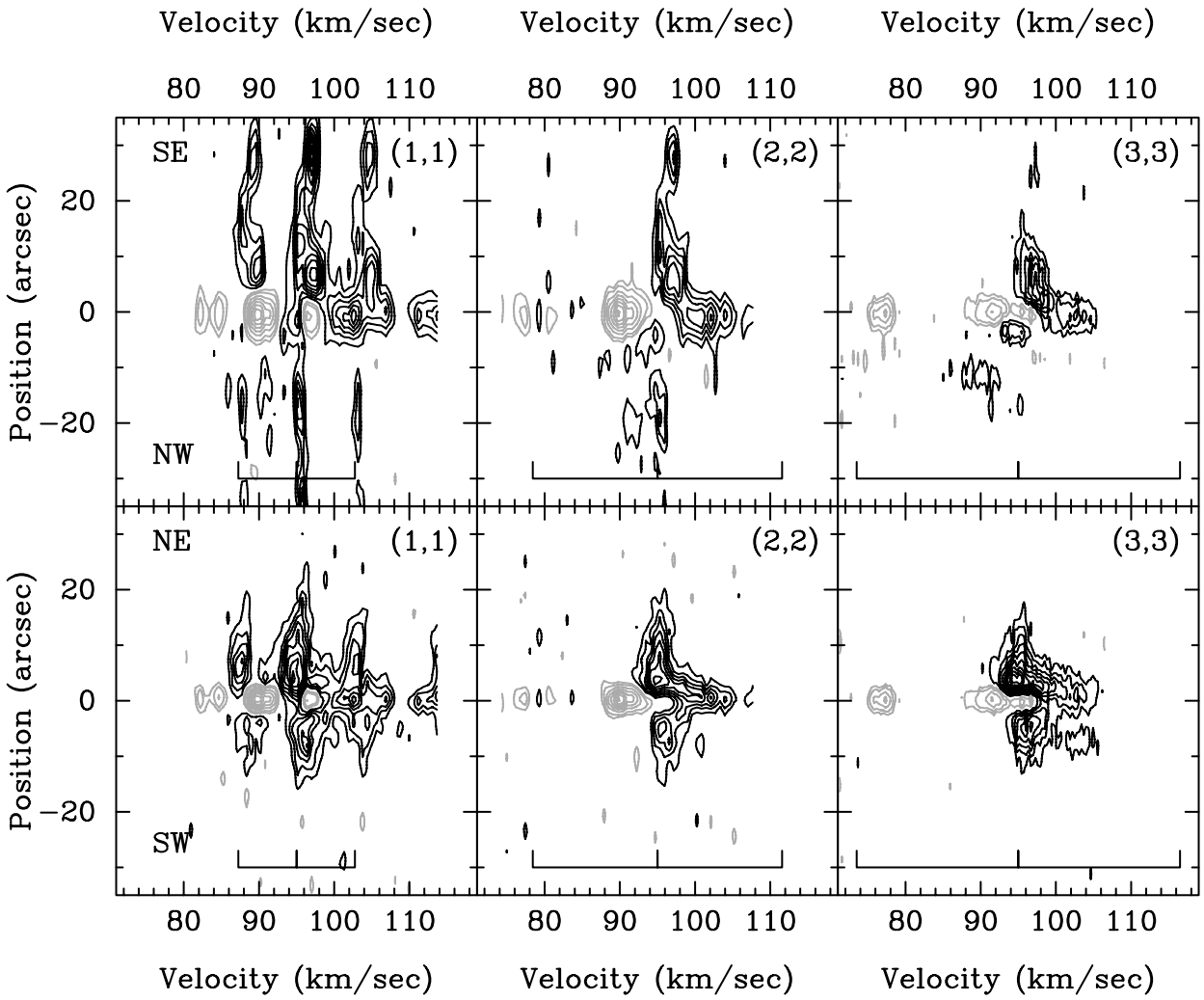

FIG. 8.—Position-velocity diagrams of the (1, 1), (2, 2), and (3, 3) data at 3″ resolution. The gray contours are −10, −8, −6, −4, −2, and −1×10 mJy beam^{-1}. The black contours are 1, 2, 3, 4, 5, 6, 7, 8, 9, and 10×10 mJy beam^{-1}. All cuts go through the UC H II region at the origin where absorption is visible against the continuum. In the top row the cut goes from northwest (negative) to southeast (positive) and includes the more extended emission. In the bottom row, the cut goes through the two emission peaks (see Fig. 7) from 30° west of south (negative) to 30° east of north (positive). In all cases, position is positive to the east and negative to the west so that the position axis increases with increasing right ascension. The position of the two inner satellite hyperfine components is indicated at the bottom of each panel relative to 95 km s^{-1}. In the (1, 1) line, the main line and both inner satellite lines are included in the bandpass. In the (2, 2) and (3, 3) lines, the velocity difference between the main line and the inner satellite is much larger than for the (1, 1) line. Thus, in the (2, 2) and (3, 3) data, the spectral window is shifted to lower velocity in order to include one satellite line in the bandpass.

(2, 2) and (3, 3) are 0.25 and 0.05, respectively, giving a rotational temperature of 20 K, where we have assumed the filling factors are equal to 1 for both lines. This is consistent with the upper limit of 30 K for the temperature of the outflow component, derived from the high-resolution data. The fact that the back side of the outflow is only detected at the position of the UC H II region implies that it is no larger than the synthesized beam. The outflow cannot be too much smaller than the beam, however, since the emission from the back side of the outflow is strong, reaching a brightness temperature of 16 K in the (3, 3) line, since emission much smaller than the beam will be strongly beam diluted.

The low angular resolution data also give a hint of the existence of the infall component, but only in the satellite lines, and mainly in (3, 3), emphasizing the high optical depth and temperature of the infall component. The satellite is only barely detected in absorption in (2, 2), but in (3, 3) it is strongly detected. Since the intrinsic line strength of the inner satellite in the (3, 3) line is only about 3% of the main line, detecting the inner satellite strongly means the optical depth of the gas must be very high. The satellite absorption is at 75–78 km s^{-1}. Since the (3, 3) satellite line is offset by 21.5 km s^{-1} from the main line, the corresponding high optical depth absorbing material should appear in the main line from 96.5 to 99.5 km s^{-1}, exactly the velocities at which we detect the infall component at higher resolution (see Fig. 4 especially). But if the optical depth toward the UC H II region is so high from 95 to 100 km s^{-1}, why does the position-velocity diagram show little absorption and even some emission in that velocity range at the position of the continuum source? This apparent contradiction does not mean that the satellite line is somehow wrong in predicting the presence of optically thick main-line absorption. Instead, in this low spatial resolution data where the synthesized beam is larger than the continuum source, line emission in the range 95–100 km s^{-1} from the area near the UC H II region can fill in the absorption that would otherwise be dominant.

In the low-resolution data there are two clumps detected in all three lines, one northeast, the other southwest of the UC H II region. The satellite lines are detectable in these two clumps, only in the (1, 1) line. Following the method of Ho & Townes

(1983) for determining a rotational temperature when optical depth is calculable for only one rotational state, we estimate the temperature of both clumps to be 30 K. Based on the $NH_3(1, 1)$ emission, the column densities of NH_3 are 1.2×10^{15} and 1.0×10^{15} cm^{-2} in the northeast and southwest clumps, respectively. Assuming an NH_3 abundance relative to H_2 of 10^{-7} (van Dishoeck & Blake 1998), the northeast clump contains 12 $M_\odot$ of gas, and the southeast clump contains 10 $M_\odot$.

4. DISCUSSION

4.1. *The Model*

There are six key observational results that any model of this source must include. First, there must be two components, an infall component and an outflow component. Second, the outflow component must be seen in absorption over the entire face of the UC H II region, while the infall component must be seen over only half, cutting off in a sharp northwest-southeast line. Third, while the velocities of the infall component show a large projection effect over the 1″ continuum source, the velocities of the outflow component do not project out nearly as strongly: that is, the velocities do not vary strongly with position and do not return to the ambient velocity at the edge of the continuum source. Fourth, the infall component must have high optical depth and a warm temperature (280 K), while the outflow component must have low optical depth and a lower temperature (20–30 K). Fifth, the outflow component must be smaller than the D-array beam, since the emission from the back side of the outflow is seen in the low-resolution data only at the position of the UC H II region. At the same time, the outflow component cannot be much smaller than the D-array beam, since the emission is not too strongly beam diluted. Sixth, the model should explain the elongated shape of the continuum source, parallel to the sharp edge of the infall component. The model that we describe here fits all of these observed results.

Figure 9 shows our preferred model for G28. The infall component and the central continuum source are an inclined, infalling, possibly slowly rotating toroid, whose central region has been ionized by the central star out to a radius of 3400 AU (0.017 pc). The toroid is similar to those proposed in Beltrán et al. (2005). The ionized gas may resemble the photoionized disks modeled in Hollenbach et al. (1994) except that in this case there is no rotationally supported disk, just the infalling toroid. The outflow component is a molecular shell swept up by a larger, more tenuous expanding bubble of ionized gas. The radius of the shell is roughly 8300 AU (0.04 pc).

Our proposed model fits all the key observational results. The infalling and slowly rotating torus can be seen against part of the continuum source, but not all of it. The rear side of the torus obviously cannot be seen in absorption. The torus is undetectable in emission in the D-array data because of its small size compared to the low-resolution beam. The outflow component provides the 88–92 km s^{-1} absorption, and the 100+ km s^{-1} emission seen at low resolution. The outflow is larger, more fully filling the beam at low resolution, and thus is detectable in emission. Because the expanding shell is large compared to the continuum source, its line-of-sight velocity does not return to the ambient velocity at the edge of the continuum source. The projection that is at work on the velocities of the infall component therefore does little to change the apparent velocity of the expanding shell. Because the infall component is closer to the central source it should be warmer than the outflow, which is mostly likely an isothermally shocked molecular shell. The infall component will naturally be more optically thick, since infalling gas is naturally centrally condensed. If the continuum emission is from photoionization of the densest central region of the toroid, that continuum emission region ought to be intrinsically flattened. Thus, the inclination needed to get the sharp edge in the first-moment map of the infall component would also naturally provide the elongation of the continuum source. In this way, the proposed model fits all of our key observational results.

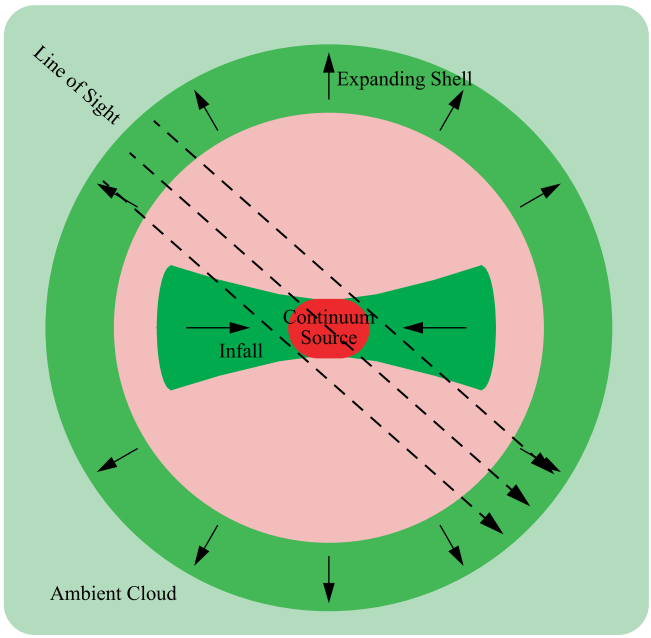

FIG. 9.—Schematic drawing of the geometry discussed in § 4. The figure shows a possible line of sight from which the proposed geometry matches the observations. Solid arrows represent motions in the molecular gas, while dashed line arrows represent lines of sight from the observer through the continuum source and absorbing molecular material.

The infall component is consistent with the existence of a central source having a mass of 79 $M_\odot$, while the infalling gas itself may include an amount of gas similar in mass. The local velocity is 95.5 km s^{-1}, and the most redshifted part of the infalling gas is at 100 km s^{-1}. We assume that this fastest infalling gas is at the radius of the continuum source, which has a deconvolved radius of 0.″6, or 3400 AU (0.017 pc). If the continuum source is intrinsically circular, then the elongation implies an inclination of 45°. Assuming the gas is in free-fall toward the central source, and all the velocity is in the plane of the disklike structure, our estimate of the central mass, given by

$$M = \frac{R(v_{\rm in} - v_0)^2}{2G\sin^2 i}, \qquad (1)$$

is 79 $M_\odot$. This is much larger than, but consistent with, the lower limits of 41 $M_\odot$, based on the ionizing flux, and 31 $M_\odot$, based on the far-IR luminosity. (If the velocity is not purely in the plane of the disklike structure, then the maximum velocity seen might be entirely along the line of sight, in which case $\sin i = 1$ and the derived central mass would be 40 $M_\odot$.) The luminosity also sets an upper limit of 31 $M_\odot$ on the largest star in the region, so this is likely to be a multiple system. This is not surprising given the high multiplicity of early-type stars (Preibisch et al. 1999). The mass seen in absorption in the infall component itself, 9 $M_\odot$, could be only a small fraction of

the mass of the toroid depending on the geometry. At the very least, the total mass is more than 18 $M_\odot$, since in absorption we only detect the near side. This is reminiscent of disklike structures seen around very young early B-type and late O-type stars, which have masses that are an appreciable fraction of the stellar mass (Beuther et al. 2004; Zhang et al. 1998a, 2002).

The outflowing molecular gas could be part of a jet-driven bipolar outflow as seen around protostars, or it could be the product of pressure-driven expansion of the H II region, or even a spherical wind. Following Keto (2002a), we calculate the Bondi radius of the ionized gas. Given the mass as derived from the infall, the radius at which gravity and thermal pressure of the ionized gas balance is 240 AU, where we have assumed an ionized gas temperature of 10,000 K. The radius of the detected continuum emission is 3400 AU (0.017 pc), so one could reasonably expect that the ionized gas is in a phase of pressure-driven expansion. This also justifies our earlier assumption of constant density in the ionized gas. However, the velocity of the outflow component is smaller than what one would expect for pressure-driven expansion. The absorption and emission seen in the low-resolution (2, 2) data are separated by a maximum of 17 km s^{-1} (88–105 km s^{-1}), so the expansion velocity is 8.5 km s^{-1}. As a sound speed, this corresponds to a temperature of 3200 K for the ionized gas. Since the ionized gas is certainly hotter than that, the expansion may be impeded by the ram pressure of an infalling envelope. Still, the gravity of the central star should be weak compared to the force of the pressure imbalance between the ionized gas and the molecular gas. The ionized gas should be undergoing dynamic pressure-driven expansion. Given a diameter of 3″, equal to the size of the D-array synthesized beam, the expansion speed implies a dynamic age of 5200 yr. But if the UC H II region had an earlier gravitationally confined stage as described in Keto (2002a), the age of the source could be much larger. Another possible explanation for the expansion velocity being smaller than the sound speed of the ionized gas is that the outflow is not undergoing purely spherical expansion, but is rather a more directed bipolar outflow. In that case, the outflowing molecular gas might not be moving just along the line of sight, but also with a velocity in the plane of the sky.

The two clumps, one to the northeast, the other to the southwest, seen in Figure 7, do not fit clearly into our model. The two clumps are separated from the UC H II region by roughly 0.2 pc (41,000 AU). Thus, on the scale of Figure 9, they are off the page. The question of how to connect the gas in those clumps to the gas seen in the high-resolution data remains, however. First we should note that if there were no high-resolution data available, we would probably have interpreted the clumps as evidence of a rotating disk. The NH_3(3, 3) emission in Figure 7 is elongated along the northeast-southwest cut and shows a velocity shift from one side of the UC H II region to the other side. This is similar to, although not quite as compelling as, the evidence for a disk in IRAS 20126+4104 (Zhang et al. 1998b). The point is moot, however, since the high-resolution data firmly establish the axis of symmetry as northeast-southwest and the plane of the toroid as northwest-southeast. Since the toroid is seen in the high-resolution data in absorption against the southwest side of the UC H II region, we would expect a bipolar outflow to be blueshifted in the northeast and redshifted in the southwest. This is indeed the sense of the roughly 1 km s^{-1} velocity shift observed in the two clumps, as seen in Figure 8. But the 22 $M_\odot$ observed in the two clumps is a great deal of mass for the outflow to accelerate. If the low velocity of the clumps is just a projection effect and we believe that the entire 22 $M_\odot$ is expanding with the same three-dimensional speed as the outflow component seen at high resolution, i.e., 8.5 km s^{-1}, the total momentum of the outflow would be 190 $M_\odot$ km s^{-1}. Alternatively, we could associate the two clumps with the infall component instead. In that case, the blueshifted clump in the northeast would be on the far side, and the redshifted clump in the southwest would be infalling on the near side. But the elongation is perpendicular to the elongation we expect from the geometry of the torus seen at high resolution. There are several ways to interpret the two clumps, none without problems. It should be remembered, however, that these clumps are beyond the physical size of the model and need not detract from the fact that the model explains all the other observed results.

We have considered and ruled out another possible model, that there are two physically distinct continuum sources, each with its own associated molecular gas, which, in projection, overlap on the sky. This model is suggested by several facts. First, the continuum source is slightly resolved into two peaks. Second, the two components of the molecular material are quite distinct. Third, it quite naturally accounts for the sharp edge in the 97 km s^{-1} as an edge in the continuum, not in the absorbing material. In this two-component model, the rear continuum source is absorbed by the 97 km s^{-1} component, and a second, nearer continuum source is absorbed only by the 90 km s^{-1} component. This way the 90 km s^{-1} gas is the nearest to the observer and can be seen in absorption against all the continuum. However, we rule out this model for the following reason. The 90 km s^{-1} component is seen in the low-resolution data to be paired with the 100+ km s^{-1} emission. The two must be physically connected. This would imply that the 100+ km s^{-1} emission is associated with the nearer continuum source. But if that were so, it would appear in absorption against the rear continuum source, which is not observed. For this reason, we reject this two-component model.

4.2. *Comparisons to Other Objects*

We contrast these observations to similar observations of G10.6 (Sollins et al. 2005). In that case, where accretion is proceeding toward a central group of massive young stars, there is some flattening associated with rotation in the molecular gas. But there is no conspicuous edge like the one we see in G28. In G10.6, the lack of a sharp edge is cited as evidence that no rotationally supported, geometrically thin, optically thick disk exists around the stellar group. While G28 does show such a sharp edge, it also does not appear to have a rotationally supported disk. The circular rotation velocity implied by a 79 $M_\odot$ central mass at a radius of 3400 AU with an inclination of 45° would be 3.2 km s^{-1}, implying a 6.4 km s^{-1} shift in velocity from one side of the UC H II region to the other. There is in fact less than 1 km s^{-1} difference in velocity across the UC H II region. So the sharp edge cannot come from the fact that the gas has settled into a geometrically thin disk. The flattening seen could come from an initially flattened geometry of the cloud, as modeled in Hartmann et al. (1996), collapse along magnetic field lines, or sculpting of the infall component via interaction with the outflow.

There are some similarities and also a key difference between G28 and other young massive stars observed to have molecular gas in disklike structures. IRAS 20126+4104, IRAS 18089−1732, and AFGL 5142 all include early B-type or late O-type stars surrounded by a rotating disk at roughly 5000 AU scale (Zhang et al. 1998b, 2002; Beuther et al. 2002). These rotating disks are sub-Keplerian and do not appear to be rotationally supported, similar to our model of G28. In G192.16−3.82, Shepherd &

Kurtz (1999) find rotation in water maser spots at radii as small as 1000 AU, also around an early B-type star. In that case, at smaller radii, the velocity gradient is consistent with Keplerian rotation. In all these cases, the amount of mass associated with the disklike structure is smaller than, but comparable to, the estimated mass of the central object. While G28 has a much more massive central object than any of these other regions, it seems to have much in common. The toroid through which infall is proceeding is not rotationally supported at a radius of 3000 AU. We detect 9 $M_\odot$ of molecular gas in absorption in the infall component, but that is just in the part of the toroid that lies directly in front of the continuum source. Certainly there must be as much mass in the part of the toroid behind the continuum source as there is in front, and depending on the geometry of the toroid, the mass might be a factor of a few larger than the measured 9 $M_\odot$. Thus, the mass of the toroid may be the same order of magnitude as the central object, similar to the other objects. Unlike any of these other objects, however, G28 has a strong central bremsstrahlung continuum source. This difference may be attributable to the larger mass, and therefore larger ionizing flux of the central star or stars. G28 could also be a more evolved version of these other sources, with more time allowing for the evolution of an UC H II region. G28 is in some ways similar to IRAS 20216+4104 and other similar young massive stars with disks, but the central source in G28 is more massive, and the system may be somewhat more evolved.

5. SUMMARY

We propose a qualitative model for the source G28.20−0.05. The model has two components: an equatorial toroid of infalling molecular gas in which a central dense region has been photoionized to form the UC H II region and an expanding molecular shell of larger radius, roughly 8300 AU (0.04 pc). Observationally, the molecular gas is easily divisible into two kinematically and physically distinct components. One is seen in blueshifted absorption and redshifted emission, with low temperature (20–30 K) and relatively low optical depth that we associate with the outflow. The other is seen only in redshifted absorption, with much higher temperature (280 K) and much higher optical depth [up to more that 45 in the (3, 3) line], which we associate with the infall. We calculate that the central mass responsible for the infall is 79 $M_\odot$ and that the mass of the torus is at least 18 $M_\odot$. The lack of strong rotation shows that, although the infalling gas has a flattened geometry, no rotationally supported accretion disk exists at radii as small as the continuum source, about 3000 AU.

APPENDIX

OPTICAL DEPTHS

We calculate two different types of optical depth in the inversion lines of NH_3 (for an example, see Fig. 10). The first we call "apparent optical depth," and it is found in any given channel by solving

$$T_{\rm line} = T_{\rm cont}(1 - e^{-\tau_{\rm app}}) \tag{A1}$$

for $\tau_{\rm app}$, where $T_{\rm cont}$ is the temperature of the continuum emission and $T_{\rm line}$ is the depth of the line absorption. This equation assumes no line emission, only absorption. For a given continuum level, the lowest calculable apparent optical depth is set by the detection of absorption as different from the continuum level, and the highest calculable apparent optical depth is set by detection of flux in the channel in question. Apparent optical depth includes a filling factor, so that a very clumpy gas with locally high actual optical depth may have a low apparent optical depth if the optically thick gas does not completely fill the synthesized beam. Apparent optical depth can be calculated wherever absorption is detected against the continuum, and a lower limit can be derived in any channel in which the continuum is absorbed down below the detection limit. For a continuum level of 100 mJy beam^{-1} and noise level in one channel of a spectrum of 4 mJy beam^{-1}, if we use 2 σ as our detection limit, the highest and lowest detectable apparent optical depths are 2.5 and 0.08, respectively. In this case, if the apparent optical depth were higher than 2.5, it would be indistinguishable from infinity, and if the apparent optical depth were less than 0.08, the absorption would be undetectable.

The second type of optical depth we calculate we call the "hyperfine optical depth." This is the optical depth of the main hyperfine component as calculated from the ratio of the fluxes of a satellite hyperfine component to the main hyperfine component. Assuming LTE, and that exactly the same material emits both the main hyperfine component and the inner satellite, the only difference in the optical depths of the two lines should be due to their differing intrinsic line strengths. Since their optical depths differ by a known multiplicative constant, $\tau_{\rm sat} = x\tau_{\rm main}$, the ratio of the fluxes of the two lines can be used to solve for the optical depth of either line using

$$\frac{T_{\rm sat}}{T_{\rm main}} = \frac{1 - e^{-\tau_{\rm sat}}}{1 - e^{-\tau_{\rm main}}} = \frac{1 - e^{-x\tau_{\rm main}}}{1 - e^{-\tau_{\rm main}}}. \tag{A2}$$

By convention, we solve for $\tau_{\rm main}$. The details of this calculation and the hyperfine structure of the different NH_3 inversion lines are laid out in Ho & Townes (1983). Because only the ratio of fluxes or temperatures is used, the hyperfine optical depth can be calculated either when the line is seen in emission or when the line is seen in absorption. Moreover, the use of the ratio means that the filling factor cancels leaving the hyperfine optical depth a truer measure of the optical depth. The detectable range of hyperfine optical depths varies between lines, since the hyperfine structure is different in different rotational states. For the (2, 2) line as seen in absorption against a continuum brightness of 100 mJy beam^{-1}, a noise level of 4 mJy beam^{-1} in one spectral channel, and using a 2 σ detection limit, the best-case scenario range of detectable hyperfine optical depths is 0.5–38. For (3, 3) the range would be 2.5–80. It should be noted that, in order to calculate the hyperfine optical depth, both a satellite and the main hyperfine components must be detected. Since the satellite line has an intrinsically lower optical depth, it is sensitive to much larger column densities of gas than the main component. In

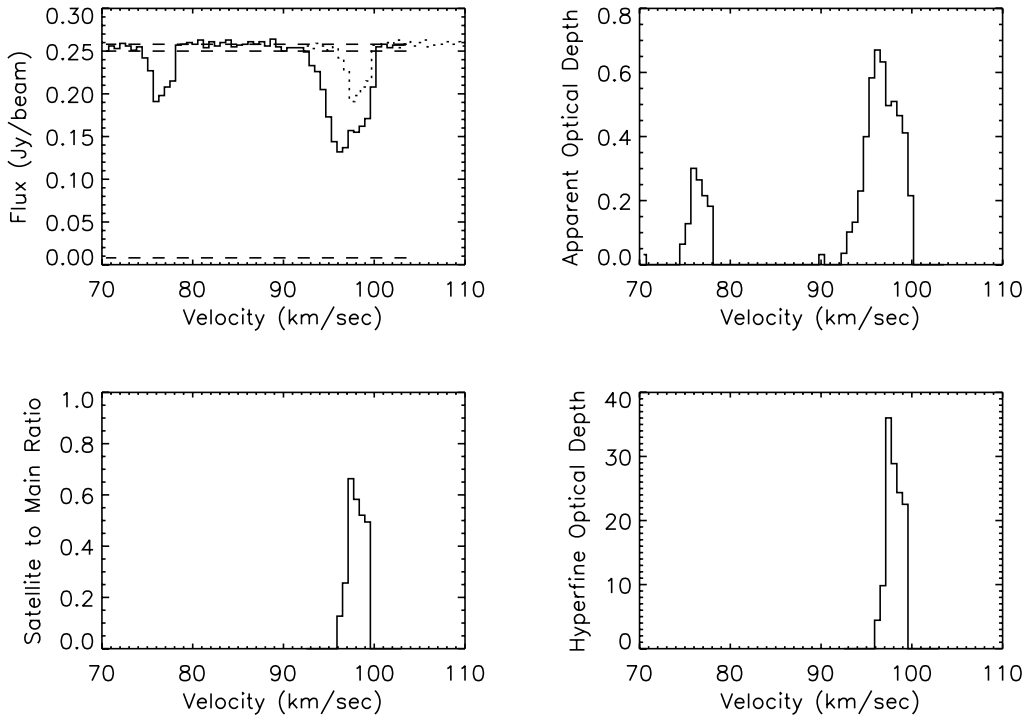

FIG. 10.—Sample BnA-array spectrum of $NH_3(3, 3)$ from G28.20−0.05, with the calculated satellite to main hyperfine component ratio, and the apparent and hyperfine optical depths. The top left panel shows the actual spectrum. The dashed lines show the continuum level at 0.258 Jy beam^{-1}, the continuum level minus 2 σ at 0.250 Jy beam^{-1}, and the lower detection limit at 2 σ, 0.008 Jy beam^{-1}. The dotted line shows the same spectrum shifted by 1.71 MHz, which is the difference in rest frequency between the main hyperfine component and the inner satellite hyperfine component. The top right panel shows the apparent optical depth. The bottom left panel shows the line ratio calculated for those channels in which both hyperfine components are detected. The bottom right panel shows the resulting hyperfine optical depth as calculated for the main hyperfine component.

some cases the satellite may be detectable in absorption, but the main line may not; for instance, if the continuum source is smaller than the synthesized beam, and widespread, low optical depth emission in the main line fills in the absorption, as in our lower spatial resolution $NH_3(2, 2)$ and $NH_3(3, 3)$ data. In this case, the hyperfine optical depth is not formally calculable. But one can get an estimate by noting that the apparent optical depth in the main line should just be the apparent optical depth of the satellite times the constant x. In almost every real circumstance, the apparent and hyperfine optical depths probe disjoint parts of parameter space.

REFERENCES

Beltrán, M. T., Cesaroni, R., Neri, R., Codella, C., Furuya, R. S., Testi, L., & Olmi, L. 2005, A&A, 435, 901
Beuther, H., Schilke, P., Sridharan, T. K., Menten, K. M., Walmsley, C. M., & Wyrowski, F. 2002, A&A, 383, 892
Beuther, H., et al. 2004, ApJ, 616, L31
Casoli, F., Combes, F., Dupraz, C., Gerin, M., & Boulanger, F. 1986, A&A, 169, 281
Chini, R., Hoffmeister, V., Kimeswenger, S., Nielbock, M., Nürnberger, D., Schmidtobreick, L., & Sterzik, M. 2004, Nature, 429, 155
Fish, V. L., Reid, M. J., Wilner, D. J., & Churchwell, E. 2003, ApJ, 587, 701
Garay, G., & Lizano, S. 1999, PASP, 111, 1049
Hartmann, L., Calvet, N., & Boss, A. 1996, ApJ, 464, 387
Ho, P. T. P., & Haschick, A. D. 1986, ApJ, 304, 501
Ho, P. T. P., & Townes, C. H. 1983, ARA&A, 21, 239
Hollenbach, D., Johnstone, D., Lizano, S., & Shu, F. 1994, ApJ, 428, 654
Kahn, F. D. 1974, A&A, 37, 149
Keto, E. 2002a, ApJ, 568, 754
———. 2002b, ApJ, 580, 980
———. 2003, ApJ, 599, 1196
Keto, E. R., Ho, P. T. P., & Haschick, A. D. 1987, ApJ, 318, 712
———. 1988, ApJ, 324, 920
Preibisch, T., Balega, Y., Hofmann, K., Weigelt, G., & Zinnecker, H. 1999, NewA, 4, 531
Shepherd, D. S., & Kurtz, S. E. 1999, ApJ, 523, 690
Shu, F. H. 1977, ApJ, 214, 488
Shu, F. H., Adams, F. C., & Lizano, S. 1987, ARA&A, 25, 23
Sollins, P. K., Ho, P. T. P., Keto, E., & Zhang, Q. 2005, ApJ, 624, L49
Terebey, S., Shu, F. H., & Cassen, P. 1984, ApJ, 286, 529
Vacca, W. D., Garmany, C. D., & Shull, J. M. 1996, ApJ, 460, 914
van Dishoeck, E. F., & Blake, G. A. 1998, ARA&A, 36, 317
Walsh, A. J., Macdonald, G. H., Alvey, N. D. S., Burton, M. G., & Lee, J.-K. 2003, A&A, 410, 597
Wolfire, M. G., & Cassinelli, J. P. 1987, ApJ, 319, 850
Zhang, Q., Ho, P. T. P., & Ohashi, N. 1998a, ApJ, 494, 636
Zhang, Q., Hunter, T. R., & Sridharan, T. K. 1998b, ApJ, 505, L151
Zhang, Q., Hunter, T. R., Sridharan, T. K., & Ho, P. T. P. 2002, ApJ, 566, 982